

This is the accepted manuscript made available via CHORUS. The article has been published as:

Precessive sand ripples in intense steady shear flows

Juan M. Restrepo, Derek E. Moulton, and Hermann Uys

Phys. Rev. E **83**, 031305 — Published 16 March 2011

DOI: [10.1103/PhysRevE.83.031305](https://doi.org/10.1103/PhysRevE.83.031305)

Precessive Sand Ripples in Intense Steady Shear Flows

Juan M. Restrepo,^{1,2} Derek E. Moulton^{1,4} and Hermann Uys³

¹*Department of Mathematics,* ²*Department of Physics, University of Arizona,*
Tucson, AZ 85721, ³*NIST Boulder Laboratories, Boulder, CO 80305, US,*
and ⁴*OCCAM, Institute of Mathematics, University of Oxford, Oxford, UK*

We describe experimental observations of fully developed, large-amplitude bars under the action of a shearing fluid. The experiments were performed in an annular tank filled with water and sheared above by a steady motor source. The same steady shearing flow can produce a variety of different erodible bed manifestations: *advective* or *precessive* bars, which refer to bar structures with global regularity and a near-steady precession velocity; *interactive* bars, whose structure depends on local rearrangements which are in turn a response to complex background topography; and *dispersive* bars, which are created when an initially isolated mound of sand evolves into a train of sand ripples. Of these the most amenable to analysis are the precessive bars. For precession bars we find that the skin depth, which is the non-dimensionalized mean-field transport rate, grows exponentially as a function of the shear velocity. From this we arrive at an analytical expression that approximates the precession speed of the bars as a function of shear velocity. We use this to obtain a formula for sediment transport rate. However, in intense flows the bars can get large engendering boundary layer separation, leading to a different dynamic for bar formation and evolution. Numerical flow calculations over an experimentally-obtained set of precessive bars are presented and show that classical parameterizations of mass flux in terms of bottom gradients have shortcomings. Within the range of shear rates considered, a quantity that does not change appreciably in time is the aspect ratio, which is defined as the ratio of the average bar amplitude, with respect to a mean depth, to the average bar length.

PACS numbers: 47.57.Gc

I. INTRODUCTION

Pattern formation in granular matter driven by hydrodynamic forcing can be classified through a series of dichotomies, pertaining to the nature of the forcing, its temporal symmetries, the mechanisms of transport, and the significance of nonlinearities. Perhaps the most obvious distinction of context is between aeolian (wind-driven) [1–4] and fluvial (water-driven) [5]. This has relevance to the relative importance of forces experienced by individual grains [6] and the structure of the nonlocal relationship between the profile of the granular surface and the local shear stress. (Reptation under steady flow conditions, for example, plays a lesser role in the fluvial case because of the higher viscosity of water, when compared to the aeolian situation). This relationship has been the subject of theoretical investigations in the context of fluid dynamics [7–9]. The temporal symmetry of the forcing, whether steady [10, 11] or oscillatory [12–16], has a clear impact on the symmetry of the patterns and the overall transport of material [17]. The distinction between suspended sediment and bedload is a key one in determining the actual dynamics of sediment transport [6], and the regime of bedload transport has received much attention in the recent physics literature [18–20]. Finally, there is the dynamical distinction between the nature of the linear instability of the planar surface and the fully-nonlinear dynamics of large-amplitude ripples.

In contrast to studies that focus on the linear instability of ripples, our emphasis is on the nature of the fully-developed nonlinear ripples that appear under steady shear. We focus on the case of steady shear in an annular

tank, the apparatus consisting of a pair of large, concentric plexiglas cylinders forming a quasi-one-dimensional chamber in the annulus. It is based on a smaller version first constructed in collaboration with S. Gubser [21], and of the type used later by Rehberg et al. [11] in the study of the linear instability of a flat layer and ripple formation [22]. Of particular relevance to the present paper is the study by the same group, [23], in which they consider the long time behavior of ripples. The primary difference in our experimental setup is much larger tank dimensions, which as we show can have a significant effect. Interest in devices with this geometry derives from the simplifying features that the complex free-boundary problem of the air-water interface, which in theoretical treatments introduces great complexity or is replaced by a prescribed free surface, simply becomes a fixed-height, fixed-velocity boundary condition at the rotor, and that end-effects are eliminated because of the periodic boundary conditions. Of course, the side walls and rotor introduce control issues of their own, discussed below. Nevertheless, the fluid and sand dynamics are sufficiently constrained that a theoretical treatment would appear to be tractable.

For intense shearing flows the theoretical treatment would have to take into account that the same steady shearing flow can lead to a variety of different types of erodible structures. The simplest of these we call precessive or advection-dominated bars. We will give a descriptive analysis of these precessive bars, but we will also take the opportunity to show, however briefly, other types of bar structures. Figure 1 shows the space/time evolution of precessive bars. The bed was prepared to be as flat as possible. A considerable amount of time

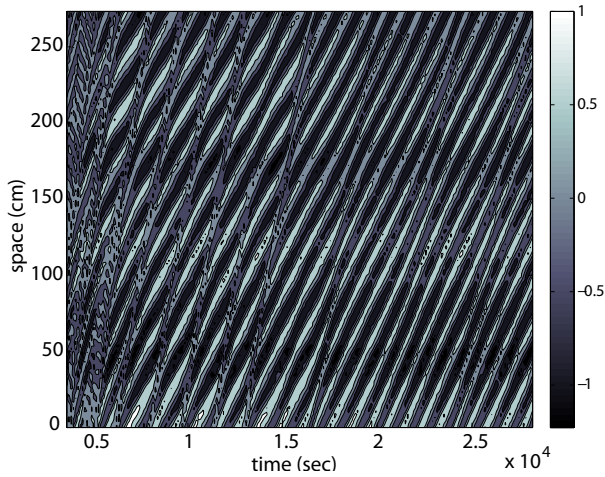


FIG. 1: (Color online) Space/time contour plots illustrating simple precession ripples. The bars gain and lose sand in time, however, their characteristics do not alter much even over long periods of time. The bar speed depends on the shear velocity but more directly on the amount of sand flux due to the shearing. The shear flow is directed upward in the figure. Toward the left of the figure we see some of the initial unsteady topographical configuration. Shown here is the time frame 3600-28200 sec. Rotor speed: 159 cm/s, rotor height: 10 cm, P140 sand.

passes before the precessive bars, with a particular precession velocity, take over. In the figure one can see (on the left) evidence of a slower and more disorganized topographic state, which then gives way to a more permanent and regular state. When preparing the initial bottom configuration the small perturbations are easily removed, but channel-length trends, however small, are not. The larger scale gradients are persistent and can be seen in experiments that take weeks or more to perform. The advectively-dominated bars have a very regular shape, moving in time at a steady rate, which in turn depends on the fixed shearing velocity. Their amplitude and length shows considerable regularity, and thus their evolution and maintenance is largely derived from uniform erosion due to steady shearing in a tank that imposes periodic spatio-temporal constraints. Precessive bars are the most common experimental outcomes when the erodible bed is prepared initially to be as level as possible.

Two examples of different topographical configurations will be shown later: an interaction case in which the sand flux is different, depending on the mean bottom topography gradient, and an example of dispersion, in which sand is collected into a mound, which when sheared will produce a downwind bar system, each bar in the system affecting the next, smaller ones downwind.

Even under very controlled experimental conditions the variability of the data was high, hysteretic. A near-constant of motion in the experiments was the ratio of the height of the bars to their lengths, even across different sand sizes and different fixed shearing speeds. Fischer

et al. [24] have noticed the significance of this height to length ratio in the context of desert dunes and denote it the *shape parameter* ϵ . Below we will define this topographical ratio and call it the *aspect ratio*, to distinguish it from the differently-defined shape parameter of Fischer *et al.*

II. EXPERIMENTAL APPARATUS

Two sections of plexiglas tubing (Reynolds Polymer), 0.635 cm thick, and with outside radii of 43.18 and 45.72 cm, are fused to a thick plexiglass base plate to form a watertight annular tank. An acrylic resin was poured into the chamber to a depth of 6 cm to raise the chamber floor for visualization purposes. Four CCD cameras (Sony, XC75) equipped with fisheye lenses ($f/l=3.6$ mm, f.o.v. 91 degrees) view the quadrants of the chamber through adjustable mirrors. Images from the four cameras are acquired at prescribed time intervals in rapid succession by a multi-channel frame grabber (Imagemill Technologies, IC2-VS-NDOC), under the control of Labview and Advanced IMAQ Vision (National Instruments). Some of the data was obtained with a variation of the optical capturing apparatus just described: a single 14MPixel Nikon D90 camera was pointed upwards and placed below the tank. The camera focused on a spherical mirror made of milar-covered plastic. The image was “unwrapped” and cropped to produce strips of 360° views of the data. Distortions inherent in the images, from the wide-angle lenses and geometric constraints on the placement of cameras, are removed by an image correcting algorithm developed by D. Patterson [25]. Briefly, images of a reference cartesian grid placed against the inner wall of the chamber are obtained for each camera and then used to define a nonlinear six-parameter mapping which minimizes in a suboptimal way the global norm of the distortion. Once this mapping is obtained it is then applied to every image obtained by the cameras. The ripple height is obtained from each image by examining vertical transects of the pixel images: under the assumption that the bar profile is a single-valued function, nearest neighbor pixel comparisons lead to an approximate height of the bars. This algorithm yields a piece-wise constant interpolation of the data. The interpolated data is then averaged using a 3-point filter with $2/4/2$ weights. This is then followed by a cubic spline interpolation of the data. The data files are recorded with a horizontal resolution of 0.2 cm and a vertical resolution of 0.06 cm. Figure 2 depicts the test apparatus.

The shearing of the fluid is effected by a rotor in the shape of a hoop, machined from a single sheet of Mic-6 aluminum, attached to a DC motor ME-3353 (Belden). The width of the hoop is nearly the same as the width of the annulus tank. The motor is directed by a Value-motion control card (National Instruments) and UMI-4A Universal Motion Interface. The rotor itself is attached to a large aluminum and plywood framework, designed

TABLE I: Diameter range for the various glass sphere types used in the experiments.

Type/name	Range of diameters (mm)
P140	0.025-0.035
MIL4	0.425-0.6
MIL8	0.15-0.22
MIL10	0.09-0.15
MIL12	0.063-0.106

so as to prevent racking. The rotor imparts steady shear on the fluid.

Water fills the gap between the granular material and the driving rotor. Experiments were conducted using two types of sand: monodisperse glass spheres with density $\rho = 2.5 \text{ g/cm}^3$. We used P140 (Potters Industries), as well as three different sizes of Mil-spec monodisperse glass spheres (Ceroglass). Table I summarizes the glass sphere diameter ranges of the several materials used in the experiments. For each sand, experiments were run at 5-6 different rotor speeds across the relevant and experimentally feasible range.

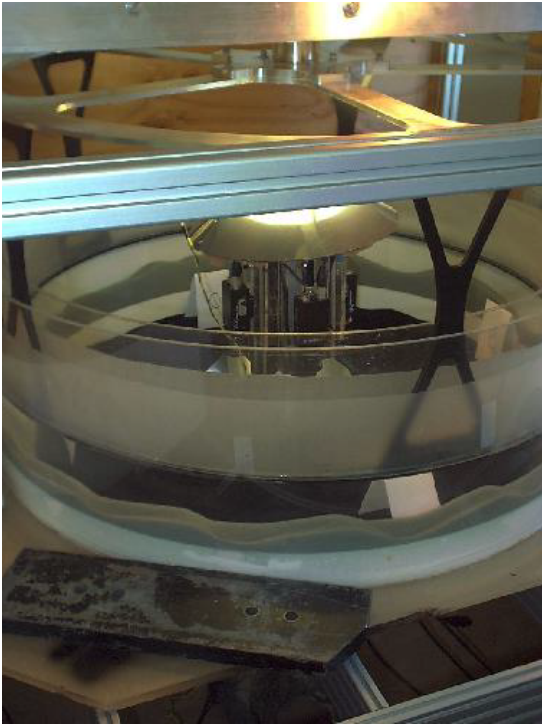


FIG. 2: (Color online) Apparatus for the study of steady-shear generated sand ripples. The X-shaped trusses connect the rotor hoop on the bottom to the motor assembly. Within the annular tank the circular rotor hoop and the light colored solid floor made of smooth acrylic resin contains the water and the glass-bead sand. Shown in the center of the figure is the image-capturing assembly.

III. OUTCOMES

The flow was fully turbulent, even when no sand was present; the Reynolds number was on the order of 10^4 . This is based on a channel width $w = 1.9 \text{ cm}$, rotor's tangential velocity $U \sim 100 \text{ cm/s}$, and kinematic viscosity of water (ambient temperature was 20°C), of $10^{-2} \text{ cm}^2/\text{s}$. In addition to the periodized geometry, there are a couple of other features of this flow that make it unlike the typical natural fluvial or aeolian setting: the tank side walls are close enough to each other and thus the wall boundary layers interact. Secondly, the solid aluminum hoop that drives the flow is close to the sand bed, so that when the bed evolves into interesting topographies significant downwind pressure gradients develop. A fundamental consequence of the first of these is that one cannot assume that the fluid flow is described by the standard plane Couette flow. In Figure 3a we depict the vertical profile of the horizontal velocity, under two different configurations: the constant shear case corresponds to the assumption that the flow is periodic in the downwind direction, has a prescribed velocity at 10 cm above a smooth bottom, no-slip at the bottom; the domain is two-dimensional and thus there are no side walls. The other case corresponds to putting two no-slip side walls, a distance of 2.3 cm apart. Figure 3b shows the estimated shear velocity

$$u_b := \sqrt{\nu \left. \frac{du}{dt} \right|_0}$$

as a function of rotor speed. Figure 3 was obtained by a full 3D Navier-Stokes computation using COMSOL. The numerical results were further checked with NEKTON5 (see [26]). We used $\nu = 8.13 \times 10^{-3} \text{ cm}^2/\text{s}$. The linear fit for the relationship between the shear velocity s and the rotor velocity r is $s = 0.1172 + 0.001197r \text{ cm/s}$. The fit has an rms error of 0.067 cm/s .

Further, though the tank radius is large the effects of curvature due to the side walls, while small, can be seen imprinted in the bars (see Figure 2). This structure evolves quickly when compared to the time scales on which the dunes advect and interact, thus making it clear what aspects of the bar morphology are due to curvature effects.

In terms of sediment motion, the experiments were in the bedload regime. This is argued as follows: The ratio of particle density to water density was approximately 2.5; particle buoyancy prevailed over time-averaged lift forces for the range of shear rates in the experiments (*cf.* [26], [27], [28]). If we estimate the settling velocity v_{settle} of an individual grain from Stokes flow drag $6\pi\eta Rv_{\text{settle}} = 4\pi\Delta\rho gR^3/3$, we find $v_{\text{settle}} \simeq 2 \text{ cm/sec}$ (for the P140 glass spheres). As we shall see, typical ripple amplitudes are several centimeters, so settling on the scale of the ripple height occurs within a fraction of a second. Particles that are launched from the top of the ripples, near where vortex separation occurs, have lat-

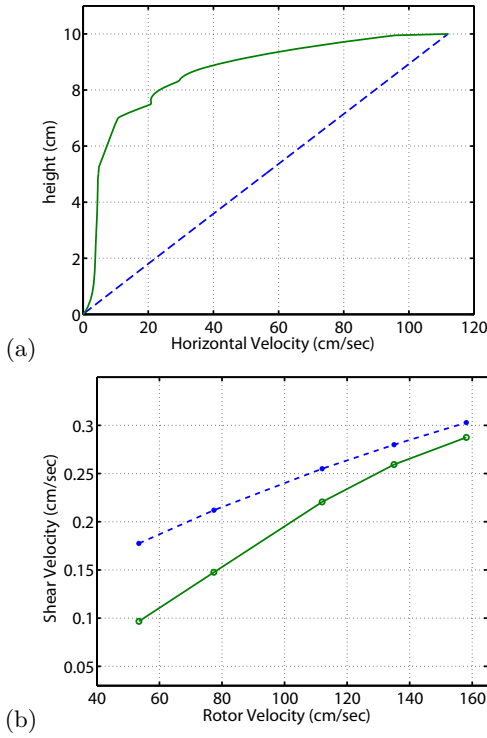


FIG. 3: (Color online) (a) The vertical profile of the horizontal velocity. Prescribed velocity at 10 cm of 1.121 cm/s, zero slip condition on the smooth bottom. Flow is periodized in the downwind direction. The linear profile corresponds to making the tank unbounded in the transverse direction. The upper curve is the horizontal velocity under the same conditions as above, but when 2 smooth zero slip side walls are added to the computation, a distance of 2.3 cm away from each other. (b) Relationship between the shear velocity and the rotor velocity; the latter is used in subsequent plots and analyses. The dashed curve is associated with the 2D calculation, the solid one to the 3D calculation (See text).

eral velocities less than v_{settle} , so they stay close to the ripples except at the very highest velocities studied. The calculation of the settling velocity in terms of the Stokes flow drag formula, in turn, is justified by the smallness of the particle Reynolds number: P140 mean diameter, the u_b , and the viscosity of water ν , this Reynolds number is about one tenth.

Prior to running the experiment we flattened out the erodible bed, as much as possible. The first few hours of data were ignored. Data was sampled every 30 seconds. Repeatability of the experimental outcome got progressively better as the shear rate increased. The shear rate range over which experiments could be performed was bounded below by repeatability issues and above by limitations of the driving motor, as well as conditions in which centripetal forces are prevalent. For low speeds the repeatability issue is related to the highly variable shear rate threshold for sand motion initiation and dislodgement. Geometry-dependent factors related to bed configuration and particle-particle geometry contributed

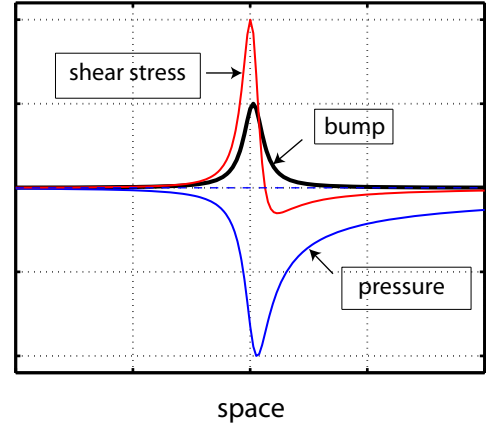


FIG. 4: (Color online) Initial bed growth and origin of bar asymmetry. Qualitative description of the stresses. A symmetric solid bump of the form $ab^2/(x^2 + b^2)$ is subjected to a linear steady shear, from left to right. Here, a and b are constants. On the surface of this symmetric bump the shear stress (top curve) and pressure, the diagonal component of the stress, (negative curve), according to Benjamin's weakly nonlinear analysis [7], are asymmetric about the bump maxima. The shear stress and the pressure depicted here are those at locations hugging the bottom topography. Amplitude and length units, arbitrary. At the bump, for low Reynolds numbers the shear is several times greater than the pressure in magnitude. As the Reynolds number gets large, their magnitude becomes similar and their role in forcing the erodible bottom equally important. Downstream from the top of the bump the shear indicates a mild flow reversal. Downstream the pressure dies off very slowly. The pressure and shear maxima are not in phase. If this symmetric bump is subjected to a sediment flux that depends on the shearing rate, as depicted here, the idealized bar will develop an asymmetric shape.

to this variability.

The time evolution of the erodible bed, starting from a mostly initially flat case to fully developed bars, has two dynamic stages: a small scale instability regime, and once there is boundary layer separation in the fluid flow, a fully nonlinear regime. Initially small defects in the sand profile encourage fluctuations in the pressure and shear stress field in the fluid and the sand. The force fluctuations occur at the locations of the topographical defects. Even when the defects on the topography are symmetric about their local maxima the bars quickly evolve into an asymmetric shape. The asymmetry is largely derived from the asymmetry of the shear stress and the pressure. The situation is well captured by Benjamin's [7] analysis, although strictly speaking applicable to laminar flows. Figure 4 illustrates the (negative) pressure and shear velocity across a symmetric bump of the form $y = ab^2/(x^2 + b^2)$, where a and b are constants. Benjamin's analysis is restricted to smooth bottom topographies and laminar near-flow conditions. The shear asymmetry will have consequences in any mass conservation statement that specifies how the fluxes are related



FIG. 5: Typical shape of the advective bars, in the long-time and fully developed flow regime. The sand has been subjected to a steady shearing flow, from left to right. The height of the bars, from trough to peak, is 2.7 cm, and the wavelength or repetition length is approximately 22 cm. The rotor velocity was 166 cm/s. Rotor height: 10.5 cm, P140 sand.

to the flow velocities/shear stresses. When the perturbations grow further the fluid streamlines separate near the crest of the bars and a different prevailing mechanism is responsible for the maintenance and evolution of the bars.

Figure 5 displays a typical sand structure, up close. In this more nonlinear regime sand is picked up at the bar crest and taken to the front of it, by vortical structures in the overlying fluid flow, that fit within the interbar spacing. These vortical structures precess, and so do the bars.

It is worth noting that there is some uncertainty in the literature as to whether the quantities bar speed, amplitude, and wavelength should continue to grow with time or saturate. In their similar experimental setup, Betat et al. [23] observed a stable saturation, although it took on the order of days for this to occur. Such saturation has not been observed in most cases in experiments in a water flume [29], [30], although the finite length of the flume plays an important role. Neither was saturation observed in the numerical simulation done by Lagr  e [31], although it is difficult to capture the nonlinearities involved in the fully developed ripples. In our experiments, saturation was observed after hours of shearing, and the quantities appearing in our figures are the average values of these saturated values.

A. Advectively-Dominated Precessive Ripples

After transients associated with the development of ripples from a flat bed die away, we find that the dominant behavior of the ripples is simple advection. In space-time portraits like Figure 1, the straight-line tracks running diagonally represent these structures. Figure 6a shows the relationship between the precession velocity and the shear velocity. Experimentally, the rotor velocity is the most easily controlled and measured variable. However, since the shear velocity is a more useful parameter, we have converted the rotor velocity to shear velocity using the linear relationship and calculations presented in Figure 3. Note that the precession velocity is very small in magnitude compared to the fluid velocity and the shear velocity; direct observation indicates that the dynamically active grains are confined to a very thin layer at the ripple surface, so the orders of magnitude difference between the precession and driving velocities is a reflection of the small thickness of this dynamic layer.

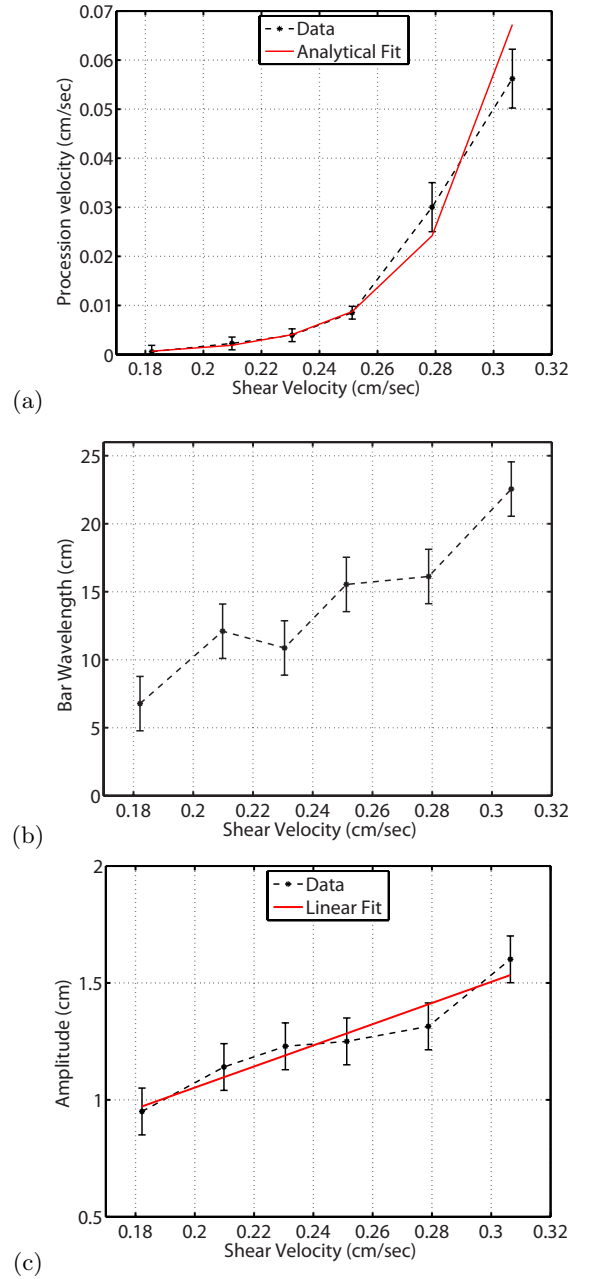


FIG. 6: (Color online) Advective bar results. (a) Precession velocity of the advection ripples as a function of the shear velocity; (b) advection ripple wavelength versus shear velocity. (c) Maximum amplitude, measured from mean-to-peak, as a function of the shear velocity. Rotor height: 9.9 cm, MIL8 sand. In this Figure and others that follow the dashed straight line connecting the data is a visual aid. The solid lines in (a) and (c) are fits to the data as discussed in the text.

The interbar spacing (or wavelength) of the advection ripples, as a function of shear velocity, appears in Figure 6b. This spacing is defined as the average repetition length (the bars have a different gradient on the stoss and the lee sides). The amplitude of the bars, as a function of the shear velocity, appears in Figure 6c. The amplitude

is defined as the average height over the mean height of the whole erodible bed, at a given time. Unlike the nonlinear dependence of the precession velocity on the shear velocity, the height and the wavelength of the bars are seen to grow almost linearly as a function of the shear velocity, suggesting a topological scaling rule for the bars. We return to this idea more fully in Section IV.

Betat *et al.*, [23] have published results on ripple formation using an experimental device similar to ours. There are significant differences between the setups, the most significant of these are the difference in size: our annular tank has a diameter roughly 3.3 times larger; and the depth of our water layer, which is roughly 7 times larger. The driver is also different: we use a hoop rotor, which affects the fluid pressure, while they use a disc. We also use different particle sizes in our experiments. As noted in [23], the effect of tank size is not well understood, and our results add another piece to the puzzle. In Figure 13 of [23], ripple amplitude and precession velocity are plotted against shearing velocity (in their case a particle Reynolds number is the independent variable, but this is equivalent to shear velocity times the scalar mean grain diameter divided by kinematic viscosity of water; hence the qualitative shape is the same). Their precession velocity curves traced out sigmoidal, S-shaped curves. This is similar to our Figure 6a, except that the velocity in most of our experiments did not level off. The reasoning behind this apparent discrepancy seems to be in the experimental ranges. We should expect the precession velocity in Figure 6a to level off at higher shear velocities, but these were inaccessible due to experimental constraints mentioned earlier. Converting the Reynolds number in [23] to a shear velocity, it should be noted that the shear velocity at which the precession velocity levels off decreases with decreased sand diameter. At our smallest-diameter sand tested, the MIL12 sand, the precession velocity *did* have the sigmoid shape, and so the results are consistent.

The biggest difference between our experimental results and those of Betat *et al.* is in the shape of the amplitude curves. They observed a sigmoid shape there as well, while we observed a roughly linear dependence for all sands. It is expected that the amplitude should not grow indefinitely, so again, there is likely a leveling off in our experiments at higher, inaccessible shear speeds (this was the case for the MIL12). However, we did not see the slow increase at lower speeds that would correspond to an S shape. This difference should be related to the quantization effect imposed by a finite length tank, which affects the wavelength and consequently influences the amplitude. This effect is amplified in a smaller system, and may be more dominant at lower shear stress, possibly accounting for the discrepancy.

Skin depth. The mechanism for precession of the bars is the result of particle mass traveling downwind. The interaction of the bars with the vortical flow generates and maintains the bars. This mass transfer is related to

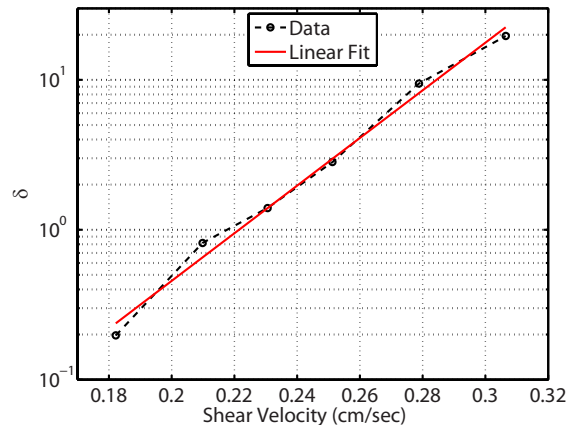


FIG. 7: (Color online) Skin depth δ , as a function of shear velocity, for advection bars. MIL8 sand, 9.9 cm rotor height.

the *skin depth*. The skin depth is defined as

$$\delta := Av_p/av_s,$$

where A is the bar amplitude, a the particle diameter, and v_p and v_s the precession and shear velocity, respectively. Hence, the skin is a nondimensional transport rate. The dependence of the skin depth on the shear velocity is illustrated in a semi-log plot in Figure 7. It is computed using the experimental mean values for A and v_p , for the $a = 0.015$ cm particle sand. The nearly linear relation between $\log \delta$ and v_s enables us to write

$$\delta av_s = Av_p = c_1 av_s e^{c_2 v_s}, \quad (1)$$

where c_1 and c_2 are constants. We can obtain a quantitative formula for the nonlinear relationship between the precession velocity v_p and the shear velocity v_s by approximating A with a linear fit as $A = c_3 + c_4 v_s$. Using the data plotted in Figure 6c, a least squares fit yields $c_3 = 0.148$, $c_4 = 4.521$. Similarly, c_1 and c_2 are obtained from Figure 7 as $c_1 = 3.008 \times 10^{-4}$, $c_2 = 36.612$. These linear fits are included in the Figures. Inserting these values into Equation (1) and solving for v_p yields a function $v_p(v_s)$ which is plotted as the solid line in Figure 6a. The 2-norm relative error in this fit is 19.3%.

The relationship between skin depth and shear velocity can also be used to obtain an analytical estimate of sediment transport rate Q in terms of shear velocity v_s . First, Q is defined by

$$Q := \sqrt{\left\langle \left(\frac{\partial h}{\partial t} \right)^2 \right\rangle} \quad (2)$$

where $h(x, t)$ is the height of the sand surface and the angled brackets denote spatial averaging (see [23]). Conservation of mass in this 1D geometry is expressed as

$$\partial h / \partial t = -\partial J / \partial x,$$

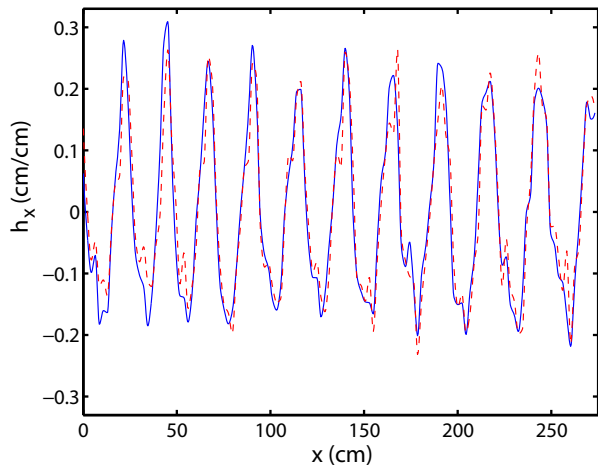


FIG. 8: (Color online) Superposition of $\partial h/\partial x$ (solid) and 40 times $\partial h/\partial t$ (dashed) at $t = 27600$ sec, corresponding to the precessive case shown in Figure 1. Note that the partial derivatives are, to within a constant, approximately the same.

where J is the mass flux. Generally speaking, J is a complex function of h as well as v_s , and perhaps moving-layer depth and microscopic (geometric factors) in order to account for fluidization events. Restricting to advectively-dominated bars, we take v_p to be constant, for a given v_s , which implies $J = v_p h(x, t)$, and thus $\partial h/\partial t = -v_p \partial h/\partial x$. To check the validity of this, we computed approximations of the time and space derivatives of h using the data connected to Figures 1, at time $t = 26700$ sec. A sample comparison of $\partial h/\partial t$ and $\partial h/\partial x$ appears in Figure 8, showing that they are roughly proportional to a good approximation. Thus, we should be able to write

$$v_p^2 \left\langle \left(\frac{\partial h}{\partial x} \right)^2 \right\rangle = Q^2. \quad (3)$$

We estimate the sand slope with a linear profile so that $\partial h/\partial x = 2\epsilon$, where $\epsilon = A/\lambda$ is the ripple aspect ratio. Hence, $Q = 2\epsilon v_p$. As we further describe in Section IV, ϵ appears to be a constant independent of shear rate for a given sand. Hence, we find that the sediment transport rate is approximately proportional to the precession velocity, and we can use Equation (1) to write Q as a function of shear velocity v_s . It seems that as the shear rate increases the depth of the layer of movable sand increases as well. The velocity profile of this layer of movable sand should decrease exponentially with depth, as is seen in granular avalanching (see [32]).

It should be noted, however, that the estimate of v_p , and accordingly the estimate of Q , are invalid if v_p levels off as expected at high rotor speed. Also, the formula for Q ignores the inherent asymmetry in the bars. Making things slightly more complex, we would have $\partial h/\partial x = 2\alpha\epsilon$, where α is a geometrical constant accounting for the asymmetry. In the case of the MIL8 sand, we computed the transport rate Q using the discrete version

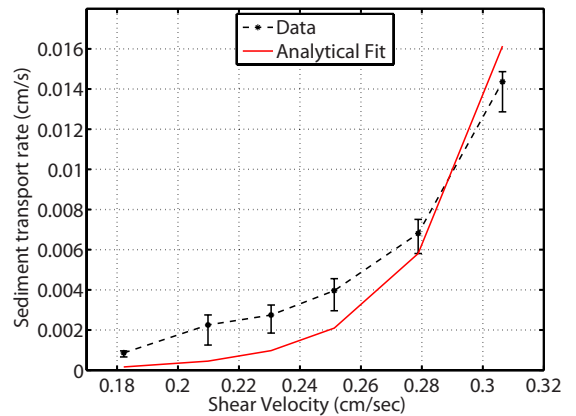


FIG. 9: (Color online) Sediment transport rate Q , assuming (3) is valid, as a function of shear velocity, for advection bars. MIL8.

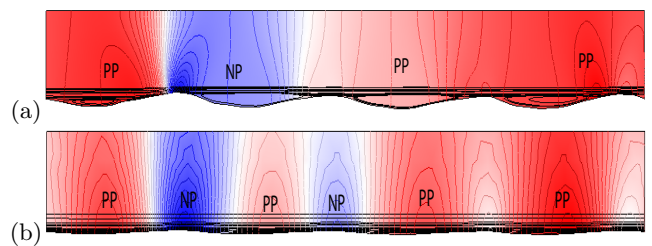


FIG. 10: (Color online) Fluid flow over a portion of the bottom topography, for the case shown in Figure 1, at time=26700 sec. The portion chosen spans from 66 cm to 168 cm. The rotor speed for this case was 159 cm/s. The rotor was located 10 cm over the bed. The flow is calculated using the steady Navier Stokes equations with no-slip boundary conditions, except that the flow was periodized in the transverse direction. In color is the pressure field: red regions correspond to positive pressure and are labeled PP, and blue is negative and labeled NP. The streamlines appear as the thick black lines. (a) Simulation using the experimental bottom topography. Of note is the clear boundary layer separation of the flow over the troughs. The range of pressure for this case is -3.10×10^{-3} to 5.40×10^{-4} Pa (b) Simulation using the same bottom topography, however, it has been scaled down in amplitude by 0.25, the amount of scaling required, other conditions being equal, to see the disappearance of the flow separation. The range of pressure for this case is -9.03 to 6.25×10^{-5} Pa.

of Equation (2). For each rotor speed, we took a fixed number of spatial points from the data, and averaged $(\Delta h/\Delta t)^2$ over multiple time steps for each point. We then computed Q as the square root of the average over the spatial points. We then compared to the formula $Q \approx 2\epsilon v_p$, where for this sand $\epsilon \approx 0.12$. The result appears in Figure 9. The general shape is consistent, though it is at best a rough approximation, with a 2-norm error of 22.7%.

Fluid flow. The analysis above made no reference to the fluid flow. To better understand possible sources of error

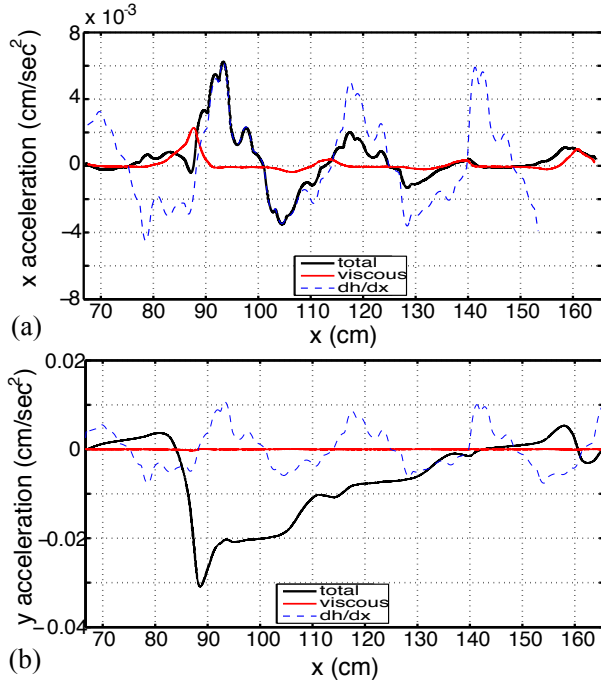


FIG. 11: (Color online) Accelerations and bottom gradient associated with the flow and bottom topography shown in Figure 10a. (a) The x-component, and (b) y-component, of the acceleration evaluated at the surface of the bottom topography. The lighter red lines correspond to the viscous components and the darker black lines to the total acceleration (viscous, plus pressure contribution). In dashed-blue we show the derivative of the bottom topography, dh/dx ; the vertical scale of the gradient is arbitrary, the actual maximum gradient was approximately 0.3.

in the preceding simple analysis, we turn next to examining the fluid flow. Figure 10a was generated numerically. It depicts the stationary solution to the Navier Stokes equations, for water over a time-steady bottom topography. The bottom topography used in the calculation is a portion of an experimentally-obtained erodible bed pattern, shown in Figure 1. The flow has been periodized at the ends. At a height of 10 cm, the fluid velocity was specified: it was a constant 159 cm/s, from left to right. No-slip boundary conditions were imposed at the bottom. Shown is the pressure field, in color, and a few of the streamlines, in black. The pressure is highest at the bar stoss side. These “form” pressure fluctuations are significant in this experimental setup due to the proximity of the rotor hoop to the sand bed. This needs to be remembered when results from this experiment are extrapolated to the situation occurring more typically in nature. Of note is the streamfunction recirculations in the troughs, indicating that boundary layer separation was taking place and thus there was an inflection point in the velocity giving way to flow reversal. Associated with Figure 10a is Figure 11, which shows the transverse (x) and vertical (y) components of the acceleration. The black curve is the total acceleration, and the red curves

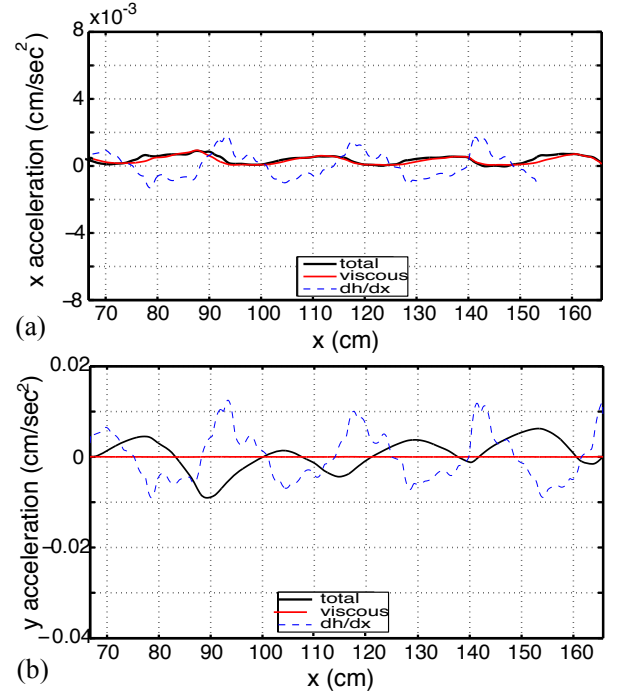


FIG. 12: (Color online) Accelerations and bottom gradient associated with the flow and bottom topography shown in Figure 10b. (a) x-component, and (b) y-component of the acceleration evaluated at the surface of the bottom topography. Bottom gradient has an arbitrary scale, but the maximum amplitude is about 0.075. See Figure 11 for comparison and for figure details.

correspond to the viscous component. The acceleration is defined as

$$-\frac{1}{\rho}p + \nu[\nabla u + (\nabla u)^\top].$$

The pressure is p , the density of water is ρ , the water viscosity is ν , the fluid velocity is u . The “viscous component” excludes the pressure contribution. Of note is that the viscous component is less significant, and that the viscous component is larger in the x -direction than the y -direction. The correspondence between the bottom gradient and the accelerations is not obvious. We also calculated the steady solution to the Navier Stokes equations for the same flow parameters, however, we scaled down the bottom topography data by 0.25. The numerical experiment we performed was to gradually reduce the amplitude of the topography, by decrements of 0.05, until we obtained no discernible flow separation. Somewhere between a scaling reduction of 0.3 and 0.25 the flow separation ceases to exist. In Figure 10b we show the resulting flow, for comparison with Figure 10a. Figure 12 shows the resulting accelerations for a gradient which is approximately 0.075, maximally. We note again that the viscous component is largest in the x direction, moreover, the viscous component is nearly entirely capturing the x component of the total acceleration in x . In the y direction the viscous component has little to no contribution

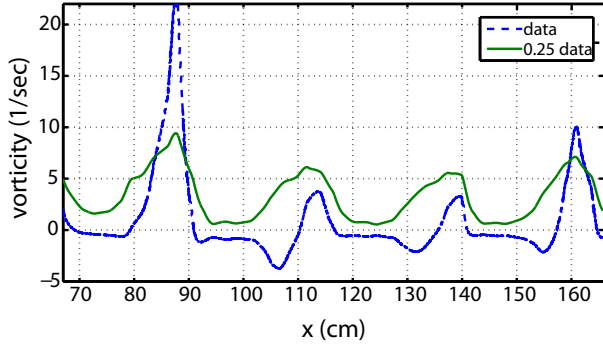


FIG. 13: (Color online) The vorticities evaluated at the bottom topography for the real and 0.25-reduced amplitude bottom topography simulation.

to the total y component of the acceleration. Of note is that in this reduced-gradient case, with no flow separation, there is, arguably, significantly more correlation between the acceleration and the gradient of the bottom topography. We also see that the x -component of the acceleration is not negative, as is the case in Figure 11.

Figure 13 shows the vorticity evaluated at the bottom topography for the real and the reduced-amplitude topography calculations. The most important difference between both cases is the existence of negative vorticity for the case associated with Figure 11. It is also clear that the vorticity is nearly entirely captured by $\partial u / \partial y$, and thus consistent with the acceleration pictures above.

These numerical calculations demonstrate the complex nature of the fluid flow once flow separation occurs at the larger bar amplitudes corresponding to higher shear stress.

B. Interaction-Dominated Ripples

The behavior of ripples dominated by *interaction* mechanisms is far more complex than the advectively-dominated counterparts. One manifestation of complexity is the local fluidization of the bed. The result is a speedup of topographic evolution (compared to the local center-of-mass speed of the whole bed). While constantly-precessing bars are on the order of centimeters in amplitude, the fluidization events lead to interaction bars of a tenth to a fifth in size. Fluidization events affect locally the inherent nature of the flux of sand. We never saw fluidization affecting the entire length of the erodible bed at a given instance in time; by the same token, it was not clear whether the events were triggered by finite-length effects of the tank: it is possible that over time the symmetries imposed by quantization deteriorate, leading

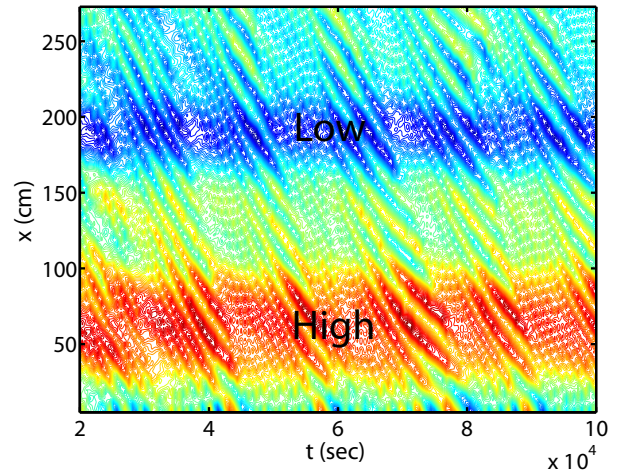


FIG. 14: (Color online) Faster interaction ripples interspersed between the slower precession ripples. Rotor speed 173 cm/s, rotor height 10.5 cm; P140 sand. Elevation is indicated by color, with red representing the highest values; the highest and lowest regions are labeled 'High' and 'Low', respectively. See Figure 15 for initial and final bed topography, as well as for height scale.

to imbalances in the fluid shear forces and a higher energetic state arises. These in turn lead to fluidization events which persist until the water/sand system reestablishes an overall lower energy balance. Another possibility is that this large scale/small scale interplay is a “granular chain reaction,” the result of a complex manifestation of the geometric stick-slip response of the bed. Many newer models for erodible beds under the action of steady shearing, such as the “minimal model” capture the saltation and/or reptation processes by adding a mass flux component with grain scale parameterizations (*e.g.*, see [24] and [33]).

Fluidization events are usually short-lived, infrequent, and unpredictable. However, when a background large-scale structure in the bottom topography is imposed, the occurrence of fluidization events is far more frequent. Figure 14 shows an example of this; the bars associated with fluidization are clearly visible and are frequent: they are the smaller and faster ones. The larger precessing bars are nonlinearly affected by the smaller ones, as mass exchanges between the larger and smaller bars force changes in the influx and outflux of the larger bars. The larger precessing bars thus change in height, wavelength and speed, as a result of the interaction. Figure 15 shows the initial and final bed topography corresponding to the portion of the experiment shown in Figure 14. Observe in Figure 15 that while the very high frequency features of the initial configuration are removed by the action of the imposed shearing flow, the final configuration remembers the large scale features; hence the ripples in the final configuration are superimposed on the larger scale structure. This accounts for the horizontal red and blue bands in Figure 14, which correspond to the maximum

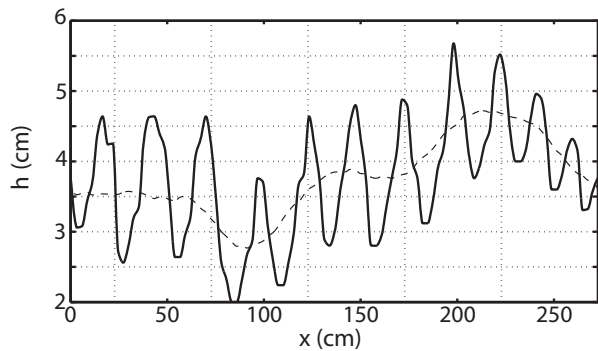


FIG. 15: Initial (dashed) and final (solid) bed topography: amplitude as a function of position. (A portion of the space-time portrait for this case is shown in Figure 14). Flow from left to right. The initial configuration of the bed was given large scale variations in height. The final configuration is pictured, after 26 hours, approximately. The initial bottom configuration persists, even after approximately 7 precession lengths. Rotor speed: 173 cm/s, rotor height: 10.5 cm. P140 sand.

and minimum locations in the initial bed topography. It was generally the case that the initial bed configuration showed little change even when subjected to intense and extensive fluid shearing, provided that the structure in the initial conditions had length scales much larger than the tank depth.

C. Dispersion-Dominated Ripples

Another topographical manifestation of the erodible material subjected to steady shear is what we call *dispersion*. One way to obtain a clean representation of the phenomenon is as follows: Sand was initially placed to form a single pile, roughly 15 cm in length and 2.5 cm in height in a tank. The rotor-to-bottom distance was 9.9 cm. The rotor was started impulsively, imparting a steady shearing force nearly immediately. The pile displayed erosion first, on the stoss side, near the top. The stoss side grew in length and the pile developed a series of bars that are roughly organized by height, downwind. Figure 16 depicts the space-time plot of the experiment, soon after the pile starts to resolve itself into a series of ripples. The smaller ripples that form part of the structure travel faster than the larger ones.

IV. PERSISTENCE OF THE ASPECT RATIO

We define the aspect ratio ϵ , as the ratio of topographic mean trough-to-peak bar amplitude to mean bar length (or repetition length). For the simple advective ripples we find that the aspect ratio is nearly constant as a function of the shearing velocity. This trend extended to different sand particle sizes, although the value of ϵ changed.

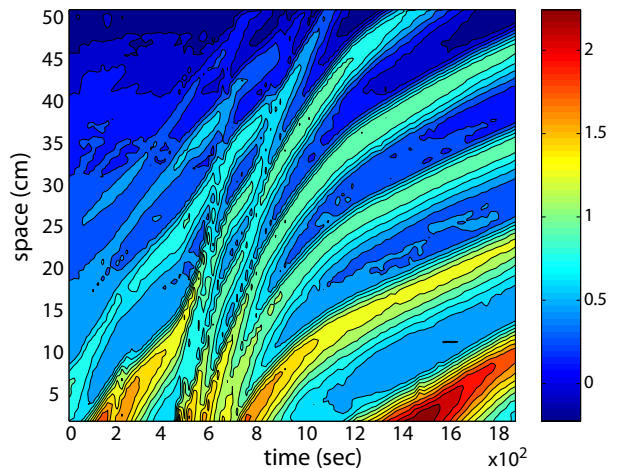


FIG. 16: (Color online) Dispersion ripples emanating from a sand pile under the action of a steady shear. Flow directed upwards in this figure. Rotor speed 142.8 cm/s. Contour heights in cm. Rotor height: 9.9 cm. P140 sand.

As mentioned in Section II, experiments were conducted with three different particle sizes of MIL-spec sand, all with similar dispersion characteristics, as well as P0140 sand. All four sands demonstrated similar behavior. In particular, the amplitude and wavelength increased linearly with shear rate, implying a nearly constant ratio of amplitude to wavelength for all sands. Figure 17 shows how ϵ depends on particle size. For the MIL-spec sand, the larger particle size leads to a lower ratio. To further explore this, we measured the avalanche angle of single piles of the MIL-spec sands, in water, shearing absent. The avalanche angles, in radians, for each of the sand

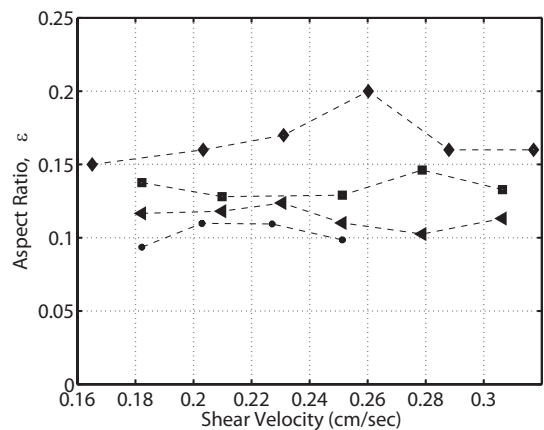


FIG. 17: Aspect ratio ϵ , defined as the mean bar amplitude (mean height to top) to length ratio, as a function of particle size. (From top to bottom): P0140 sand, with mean radius 0.025 cm (diamonds). The next sets are all Mil-spec sand of similar dispersion characteristics, MIL12, MIL8, MIL4. The error bars are omitted: the experimental uncertainty was ± 0.05 cm/cm.

sizes were: MIL4: 0.3, MIL8: 0.31, MIL12: 0.33, although it should be noted that the error associated with this measurement was about 0.02 radians. Nevertheless, the variation of the avalanche angles with particle size seems to be consistent with the variation of the ratios given in Figure 17, suggesting that the avalanche angle may be a key parameter in the size of the sand bars. The P0140 ballotini sand does not conform to this trend; its particle dispersion specifications are different.

Further evidence for the insensitivity of ϵ to shearing velocity is provided by the following experiment: we allowed the experiment to run overnight, with a rotor speed of 119.0 cm/s, developing bars from an initial flat configuration. We then changed the rotor speed to 166.6 cm/s and found that the precession velocity increased, as did the wavelength and amplitude of the bars, such that the ratio ϵ remained roughly constant. We also tried the reverse experiment, wherein we produced bars at the higher shear rate and then ran the experiment at the lower speed, leading to the opposite effect: a significant change in the precession and a decrease in wavelength and amplitude, but not in the ratio.

V. SUMMARY

In this paper we have presented the results of experiments on the fluid driven motion of fully developed sand bars and ripples under intense shear flow. An annular tank with a large circumference-to-width ratio was utilized, with shearing due to a fixed height rotor. Running the experiment over long periods of time enabled us to study the behavior and structure of fully developed ripples. However, even in this relatively constrained fluid dynamics environment and allowing for initial instabilities to develop into fully formed sand bars, the particulars of the motion are inherently complex, characterized by nonlinear behavior, transient interactions, and non-uniform motion of sand particles. Accordingly, our focus was on the larger structure, analyzing the advective speed of the ripples and pattern formation in terms of the amplitude and wavelength of sand bars.

Shortly after the flat erodible bed is subjected to shearing, bars develop on the surface, quickly developing an asymmetric shape with a distinctive steeper downwind face. This small-amplitude range of dynamics is controlled by the asymmetry in the pressure and bed shear in the fluid flow, generating in turn an asymmetric flux rate across each bar's length.

We identified three types of bar structures: advective, interactive, and dispersive. The most common type of bar structures, the precessive, advectively-dominated ones, emanated from an initially-flat bottom. These consisted of a train of uniform ripples, more or less traveling at a constant speed. Periodicity and translational symmetry leads to uniformity of the mass flux rate and near-constancy of bar phase speed. The speed of the bars is nonlinearly related to the shearing velocity v_s in-

duced by the steadily moving rotor. An approximation of this relation was derived based on two observations: (i) that the skin depth increased exponentially with v_s , and (ii) the amplitude increased linearly with v_s . The resultant formula for the bar speed agreed fairly well with the data. However, a comparison with a previous study in a similar setup [23], as well as results from our smallest sand, suggest that the bar speed should level off at higher shear velocities which were inaccessible in our setup. Interestingly, our results differed the most from [23] in the increase of amplitude at small shear speed. This is likely due to the significant difference in tank dimensions, although the exact mechanism is unclear.

Constancy of the precession speed v_p , and approximate consistency between $\partial h/\partial t$ and $\partial h/\partial x$, for a given shear velocity, suggested that the flux gradient $\partial J/\partial x$ could be expressed as $v_p \partial h/\partial x$. This was used to derive a formula for the sediment transport rate as a function of shear stress. This produced a fairly poor fit to data, especially when the shearing was intense. We conjecture that this discrepancy can be partially understood in terms of the complexity of the fluid flow. A numerical calculation of the fluid flow suggested that once the bars grow sufficiently large the boundary layer separates: the troughs of the bars are filled with a vortical flow. The calculations suggested that there is no obvious correspondence between the stresses at the surface of the erodible bed and the gradient of the bottom topography, in intense shearing.

The interactively-dominated bars are far more complex. What makes these a unique category is that the sand flux is a local quantity. While overall mass preservation is observed, bars can gain or lose sand locally and thus it is far more difficult to identify consistent coherent structures. The most predictable manifestation of these was in response to background topography. The underlying large scale structure affects, locally, the bar shape, triggering frequent fluidization events. Moreover, these large-scale but shallow features persisted over very long times: there was an inherent low-pass mechanism in the erosion of the bed. This is perhaps related to the very small thickness of the moving layer or skin depth: its thickness is related to the time scales of bar evolution. This time of evolution is longer than the time scales of particle motion and vastly shorter than the time scales over which large scale and shallow features are affected by small mass fluxes. Hence, these large-scale features will change in time, however, not significantly over the time scales over which we ran the experiments (days). The shallowness is a requirement related to the variations in shearing by the fluid in the tank: a large scale structure that had considerable height would be affected quickly due to the vastly different shearing forces it experiences. This was the case of dispersion.

An interesting feature we observed was the near-constancy of the aspect ratio, which is the ratio of the mean height to mean wavelength of the precession bars. The amplitude and the wavelength of the bars grow

nearly linearly with the rotor speed, while the precession rate grows nonlinearly with rotor speed. The value of the aspect ratio was found to depend on the size of the particles making up the erodible bed. Thus particle geometry and packing play a role. Among the three cases of MIL-spec sand, the ratio itself decreased with increased particle size, and thus seems to be connected to the avalanche angle of the sand. While further experiments may be useful to further explore/confirm these results, it remains an intriguing characteristic in the context of pattern formation. Experiments on determining the role played by the vortical flows in the high shearing range of precessive bar evolution may also prove fruitful. In intense shearing conditions the boundary layer separates and vortical flows can be seen to "fit" the interbar spacings. This, in turn, suggests that there may also be a

relationship between the bar aspect ratio and the aspect ratio of the vortices, perhaps leading to insights on how the fluid flow enters the dynamics of the evolving bed topography.

Acknowledgments

One of the anonymous reviewers was especially helpful in suggesting improvements to this paper. This work was supported in part by NSF ITR grant DMS-0113649 (JMR). JMR acknowledges the Institute for Mathematics and its Applications, where some of this work was done. Additional support was provided by a Small Grant, from The University of Arizona.

-
- [1] R. Bagnold, *The Physics of Blown Sand and Desert Dunes* (Methuen and Co., London, 1941).
 - [2] B. Andreotti, P. Claudin, and S. Douady, *Selection of dune shapes and velocities. part 1: Dynamics of sand, wind and barchans*, *cond-mat/0201103* (2001).
 - [3] B. Andreotti and P. Claudin, *Selection of dune shapes and velocities. part 2: A two-dimensional modelling*, *cond-mat/0201105* (2001).
 - [4] Y. Amaraouchene, J. Boudet, and H. Kellay, *Phys. Rev. Lett.* **86**, 4286 (2001).
 - [5] J. Allen, *Current Ripples* (North Holland, Amsterdam, 1968).
 - [6] J. Fredsoe and R. Deigaard, *Mechanics of Coastal Sediment Transport* (World Scientific, Singapore, 1992).
 - [7] T. Benjamin, *J. Fluid Mech.* **6**, 11 (1959).
 - [8] R. Bagnold, *Proc. Roy. Soc. London A* **187**, 1 (1963).
 - [9] K. Kroy, G. Sauermann, and H. Herrmann, *Phys. Rev. Lett.* **88**, 054301 (2002).
 - [10] B. Krishnappan, *J. Hydraulic Eng.* **126**, 561 (2000).
 - [11] A. Betat, V. Frette, and I. Rehberg, *Phys. Rev. Lett.* **83**, 88 (1999).
 - [12] P. Blondeaux, *J. Fluid Mech.* **218**, 1 (1990).
 - [13] G. Vittori and P. Blondeaux, *J. Fluid Mech.* **218**, 19 (1990).
 - [14] A. Stegner and J. Wesfried, *Phys. Rev. E* **60**, R3487 (1999).
 - [15] M. Scherer, F. Melo, and M. Marder, *Phys. Fluids* **11**, 58 (1999).
 - [16] J. Hansen, M. van Hecke, C. Ellegaard, K. Andersen, T. Bohr, A. Haaning, and T. Sams, *Phys. Rev. Lett.* **87**, 204301 (2001).
 - [17] J. Restrepo and G. Leaf, *J. Phys. Ocean.* **32**, in press (2002).
 - [18] J.-P. Bouchaud, M. Cates, J. R. Prakash, and S. Edwards, *J. Phys. 1 France* **4**, 1383 (1994).
 - [19] J.-P. Bouchaud, M. Cates, J. R. Prakash, and S. Edwards, *Phys. Rev. Lett.* **74**, 1982 (1995).
 - [20] A. Aradian, E. Raphaël, and P.-G. de Gennes, *Surface flows of granular materials: A short introduction to some recent models*, *cond-mat/0112227* (2002).
 - [21] S. Gubser and R. Goldstein, *Experimental study of sand ripple formation and dynamics* (1996), princeton University, unpublished.
 - [22] A. Wierschem, C. Groh, I. Rehberg, N. Aksel, and C. A. Kruelle, *European Physical Journal E* **25**, 213 (2008).
 - [23] A. Betat, C. A. Kruelle, V. Frette, and I. Rehberg, *European Physical Journal E* **8**, 465 (2002).
 - [24] S. Fischer, M. E. Gates, and K. Kroy, *Physical Review E* **77**, 031302 (2008).
 - [25] D. Patterson, Master's thesis, The University of Arizona (2001).
 - [26] J. Restrepo, P. Fischer, and G. Leaf, *Journal of Fluid Mechanics* **468**, 327 (2002).
 - [27] P. Fischer, G. K. Leaf, and J. M. Restrepo, *Journal of Fluids Engineering* **127**, 583 (2005).
 - [28] P. Fischer, G. K. Leaf, and J. M. Restrepo, *Journal of Fluids Engineering* p. 101303 (2008).
 - [29] T. Loiseleux, D. Doppler, P. Gondret, and M. Rabaud, in *Proceedings of the second international workshop on marine sandwaves and river dune dynamics* (Enschede, Netherlands, 2004), p. 200.
 - [30] V. Langlois and A. Valance, *Eur. Phys. J. E* **22**, 201 (2007).
 - [31] P.-Y. Lagrée, *Phys. Fluids* **15** (8), 2355 (2003).
 - [32] S. C. du Pont, R. Fischer, P. Gondret, B. Perrin, and M. Rabaud, *Physical Review Letters* **94**, 048003 (2005).
 - [33] P. Hersen, S. Douady, and B. Andreotti, *Physical Review Letters* **89**, 264301 (2002).